Design and characterization of variable stiffness structural joints

Qinyu Wang [a,*], Gennaro Senatore [b], Kaspar Jansen [c], Arjan Habraken [a], Patrick Teuffel [a]

[a] Chair of Innovative Structural Design (ISD), TU Eindhoven, 5600 MB Eindhoven, The Netherlands
[b] Applied Computing and Mechanics Laboratory (IMAC, ENAC), Swiss Federal Institute of Technology (EPFL), Switzerland
[c] Department of Design Engineering, TU Delft, 2628 CE Delft, The Netherlands

HIGHLIGHTS

- Design and characterization of variable stiffness structural joints to control the dynamic response of frame structures.
- The joint consists of a shape memory polymer (SMP) core and an SMP-aramid composite skin.
- Stiffness reduction of the joint core through resistive heating causes a shift of the structure natural frequencies.
- The natural frequency shift significantly reduces up to 84% of the maximum displacement under resonance loading.
- The composite skin effectively restrains the joint core deformation while having a marginal effect on viscoelastic damping.

GRAPHICAL ABSTRACT
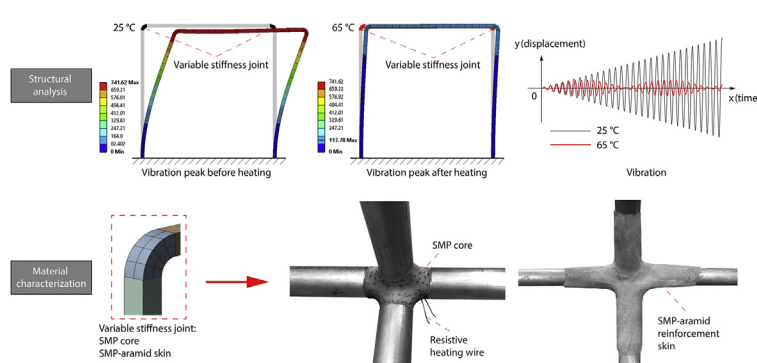
ARTICLE INFO

ABSTRACT

This paper presents design and characterization of a new type of structural joint which can vary its stiffness through actuation. Stiffness variation is employed to control the dynamic response of frame structures equipped with such joints. The joint is made of a shape memory polymer (SMP) core which is reinforced by an SMP-aramid composite skin. A controlled stiffness reduction of the joint core material, induced by resistive heating, results in a shift of the structure natural frequencies. This work comprises two main parts: 1) characterization of material thermomechanical properties and viscoelastic behavior; 2) numerical simulations of the dynamic response of a one-story planar frame equipped with two such variable stiffness joints.

The experimental material model obtained through Dynamic Mechanical Analysis has been used to carry out modal and non-linear transient analysis. However, control time delays due to heating and cooling as well as fatigue are not considered in the numerical simulations. Results have shown that through joint stiffness control, the fundamental frequency shifts up to 8.72% causing a drastic reduction of the dynamic response under resonance loading. The SMP-aramid skin is effective to restrain the joint deformation in the activated state while maintaining viscoelastic damping properties.

* Corresponding author at: Chair of Innovative Structural Design (ISD), TU Eindhoven,
P.O. Box 513, 5600 MB Eindhoven, The Netherlands.
E-mail address: q.wang2@tue.nl (Q. Wang).

1. Introduction

1.1. Adaptive structures

Structural control strategies have been classified broadly into four types: active, semi-active, passive and hybrid [1,2]. Benchmark control problems have been investigated for building structures under seismic [3,4] and wind [5] excitations. It was shown that through active control the structure response (e.g. displacement, acceleration, and inter-story drift) reduced substantially with respect to the non-controlled case. Active control systems are typically more effective to reduce the structure response but they require larger power and might cause instability [6]. Active structural control has been successfully implemented for vibration suppression of structures subjected to wind and earthquake loading [7–11]. Semi-active control systems, such as magnetorheological (MR) dampers [12], have been tested on a 20-storey benchmark building under seismic loading. Experimental results have shown that, within the context of vibration suppression, the MR damper required less energy to achieve a similar response reduction compared to active systems [13]. Passive control systems, such as base isolation, have limited capabilities compared to the other types but no power supply is required. A hybrid control system is a combination of passive, semi-active and active devices [6,14]. Applications of active and hybrid control to build structures, including high-rise buildings and bridge towers equipped with active (AMDs) and hybrid (HMDs) mass dampers, have been reviewed in Spencer & Sain [14].

Through integrated sensing and actuation, it is possible to modify the state of stress and deformation caused by external loading. This way, adaptive structures can be designed to operate closer to required limits which results in a better material utilization and a lower

Fig. 1. Shape Memory Polymer joint connected to four aluminum tubes.

'whole-life energy'. The whole-life energy is a new design criterion introduced by Senatore et al. [15] which accounts for the energy embodied in the material and the energy for control and actuation. Extensive numerical simulations on high-rise structures, bridges and self-supporting roof systems [16] have shown that well-designed adaptive structures achieve energy saving as high as 70% compared to weight-optimized passive structures. For stiffness governed problems (e.g. slender structures and/or stringent serviceability requirements), adaptive structures compete also in monetary cost terms [17]. Experimental testing has confirmed numerical predictions and the feasibility to apply this method to real structures [18].

Structural adaptation through controlled large shape changes has been employed to cause a significant stress redistribution. This way the design is not governed by peak loads that occur rarely. In this case the structure is designed to 'morph' into optimal shapes as the load changes. Numerical results and experimental testing have shown that control through large shape changes allows for a better material utilization and thus a lower embodied energy with respect to adaptive structures limited to small shape changes as well as to passive structures [19,20]. A change of geometry can also cause a significant shift of the structure natural frequencies. This strategy has been studied numerically and experimentally to mitigate the dynamic response of tensegrity structures [21,22] and for an underslung cable-stayed beam bridge under pedestrian loading [23]. Shape control has also been studied to maintain optimal performance during service. For example, shape control of aircraft wings has been implemented to reduce drag and improve maneuverability during flight [24].

Shape control requires a significant flexibility of the joints whose fixity can cause stress concentration and thus it can increase control effort. Previous work has investigated the use of variable stiffness joints to prevent stress build-up and to reduce actuation energy in order to control the structure into optimal states [25]. During shape adaptation the joints are actuated to a flexible state. After shape adaptation, the joints recover rigidity. Fig. 1 shows one of the tested joints which was fabricated using fused deposition. The joint is made of a polyurethane-based shape memory polymer (SMP) which features a large stiffness variation caused by a controlled stiffness reduction between a glassy and a rubbery state. The joint was actuated through resistive heating. Experimental testing has shown that stiffness variation under quasi-static loading is feasible [25]. It was also shown through simulations that by selectively actuating the joints of a planar Warren truss, the natural frequencies changed considerably [26]. Joint stiffness variation was simulated by releasing the rotational degree of freedom of the truss
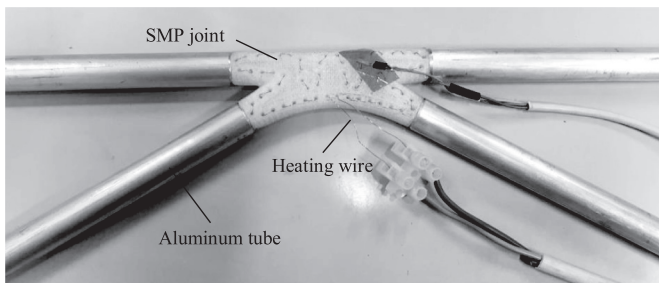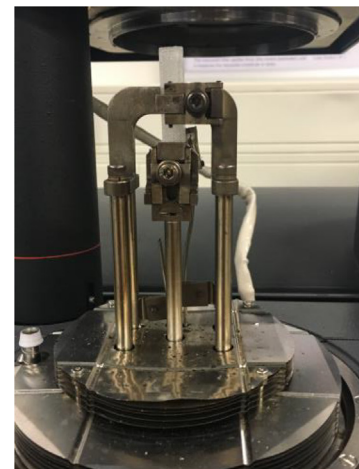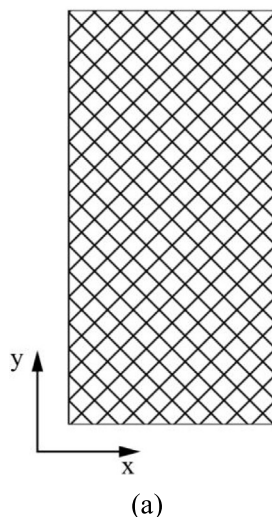

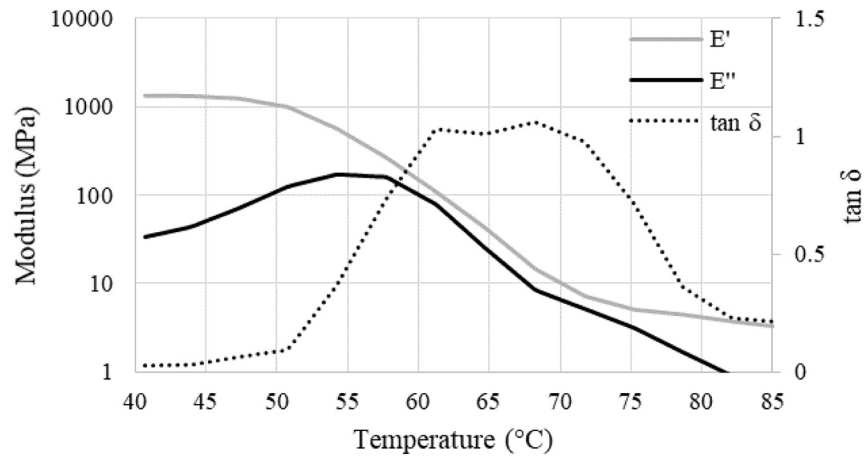**Fig. 2.** (a) 3D printed layer pattern; (b) DMA Q800; (c) specimen placement.

Fig. 3. Storage E′, loss E″ modulus, and tan δ vs temperature at 1 Hz, joint core material.

nodes. This way the joints could switch from a "locked" (e.g. a moment connection) to a "released" (e.g. pin) state.

1.2. Shape memory polymers (SMPs)

Shape memory polymers (SMPs) can recover their original shape in stress-free conditions from a deformed state through thermal, electric and magnetic actuation or by exposure to light as well as pH change [27,28]. The most widely used actuation method for SMPs is thermal actuation [29–31]. SMPs have been 3D printed through stereolithography (SLA) [32] and fused deposition modelling (FDM) [25]. For SMPs that are cross-linked, either covalently or physically, the glass transition is driven by a dual-state mechanism. Crosslinks serve as an elastic energy-storage element in the programming stage, which also drives shape recovery in the recovery stage [33]. The elastic modulus in the rubbery state is determined by the reduction of configurational entropy. Elongated polymer chains tend to return to the un-stretched random coil configuration. Above the glass transition temperature T_g, the polymer chain segments between crosslinks can deform freely which allows large macroscopic strains (up to 400%) [31]. The elastic modulus from glassy to rubbery state can reduce by up to a factor of 1000 [34–36].

SMPs composites have found several applications for the synthesis of biomaterials, solid-state actuators and smart textiles [27] as well as in aerospace engineering [37]. Actuation through shape memory alloy (SMA) embedded into an SMP composite has also been investigated for a wind-responsive façade system. The façade components change shape in order to control ventilation for indoor climate optimization [38]. However, the low mechanical and recovery stress of SMPs has limited their range of applications. To improve their mechanical properties, shape memory polymer composites (SMPC) are often integrated with particles (e.g., carbon nanotubes, Ni, Fe_3O_4, SiC), short fibers as well as continuous fibers (e.g. carbon, glass and aramid) [27,39–41]. SMPCs with particles and short fibers usually have limited mechanical properties and therefore cannot be employed for load-bearing applications. The use of continuous fibers instead significantly increases the mechanical strength and stiffness of SMPCs in the fiber (axial) direction while the shape memory effect is retained in the transverse direction [27,39,41,42]. Continuous fiber reinforced SMPCs are also more resistant to impact, crash and fatigue and hence have potential to be used for structural applications [36,37].

To simulate the thermomechanical properties of SMPs, two main models have been formulated: thermo-elastic and viscoelastic. In the first model the SMP is treated as an elastic material with a temperature dependent modulus which reduces significantly above the glass transition temperature (i.e. loss of stiffness). The second model, which is based on viscoelasticity theory [43], takes into account time and frequency dependent effects. The modulus is assumed to be time dependent, reflecting experimental records which show that in a polymer, stresses increase rapidly after loading but decrease gradually with time. This phenomenon is referred to as stress relaxation and is attributed to the molecular process of chain sliding when the material is under loading. Note that the material response under dynamic loading can be interpreted similarly: in a material which is subjected to a high strain rate or a high
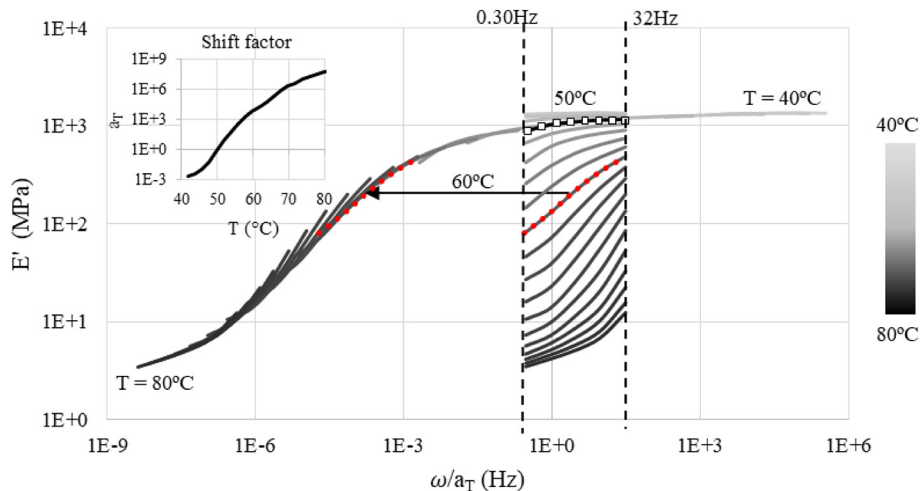

Fig. 4. Master and shift factor curves ($T_{ref} = 50\ °C$), joint core material.

Table 1
Williams–Landel–Ferry function constants for the 3D printed SMP joint core.

C_1	C_2	T_{ref}	T_g
14.6	24.2	50 °C	65 °C

frequency load, the molecules have no time to slide, resulting in a higher resistance to movement and thus a higher stiffness. Contrary, under low frequency loading chain slippage occurs and therefore there is a lower macroscopic stiffness. Material viscoelastic behavior can be measured experimentally through a series of time dependent (i.e. creep or relaxation) tests carried out at different temperatures or by dynamic mechanical analysis (DMA).

1.3. Outline

The variable stiffness joint presented in this work is made of a 3D printed SMP core and an aramid fiber reinforced SMP skin. This work unfolds in two main parts: 1) characterization of the thermomechanical properties of the 3D-printed SMP core, and a single as well as multi-ply composite laminate made of an SMP matrix reinforced by aramid fibers; 2) numerical simulations of the dynamic response of a one-story planar frame equipped with two of such variable stiffness joints. Dynamic Mechanical Analysis (DMA) tests are carried for the 3D printed SMP core and the SMP-aramid skin. The material model obtained from experimental testing is employed to carry out modal and transient non-linear analysis of a one-story planar frame equipped under resonance loading. Elastic and viscoelastic behavior are investigated. The joint is modelled

Table 2
Stiffness properties of the SMP matrix and single layer SMP-aramid composite (SMPC).

Specimens	SMP matrix	0°/90° SMPC	±45° SMPC
E_g (MPa)	1780	10400	1780
E_r (MPa)	4.2	2630	84
E_g/E_r	421	4	21
T_g	80 °C	88 °C	76 °C

with and without the reinforcement skin. Natural frequency shifts and damping properties are compared between the elastic and viscoelastic case as well between the non-reinforced and the reinforced case.

2. Characterization of the SMP core

2.1. Dynamic mechanical analysis

The joint core was made of a polyurethane-based shape memory polymer filament made by *SMP Technologies Inc.* (Tokyo, Japan). The SMP material MM-5520 is a pellet type for injection extrusion molding with a transition temperature $T_g = 55$ °C. The specimens were fabricated through fused deposition modelling (FDM) using a *FlashForge Dreamer* printer. The printing temperatures for the extruder and platform were set to 220 °C and 60 °C respectively. The specimen was printed in layers to form a parallelepiped of dimensions 20 mm × 10 mm × 1 mm; one of the layers is shown in Fig. 2(a). The infill pattern was oriented at 45° and − 45° every other layer. Each layer had a thickness of 0.01 mm. Dynamic mechanical analysis (DMA) tests were performed using a Q800

(a)   (b)   (c)
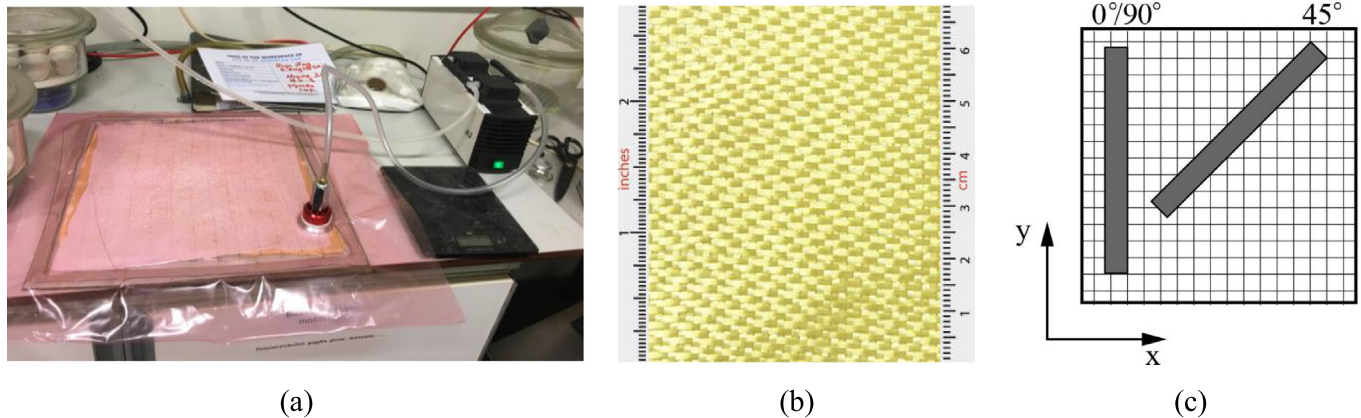
Fig. 5. (a) Aramid fabric impregnation in vacuum; (b) satin weave aramid fabric; (c) cutting directions.

(a)   (b)
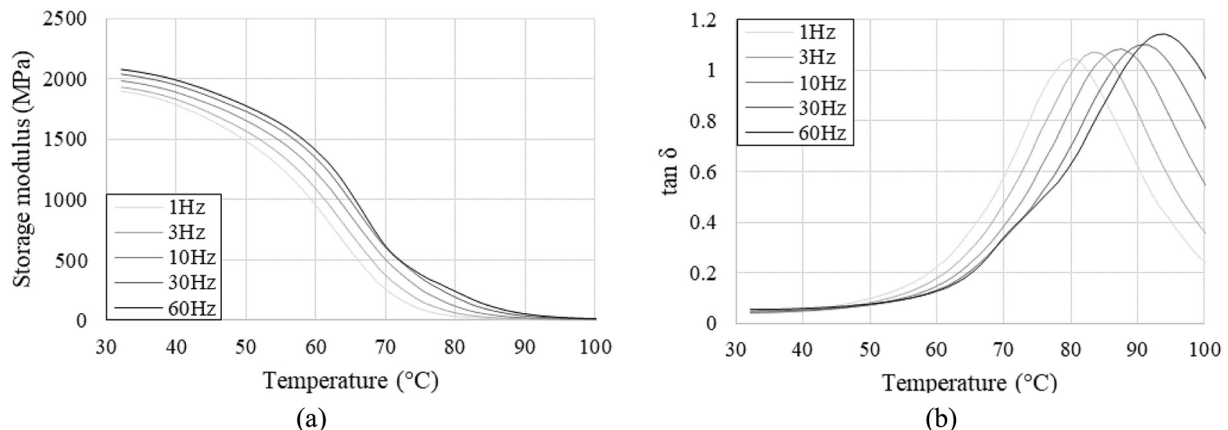
Fig. 6. (a) Storage modulus (b) tan δ vs temperature, SMP matrix without aramid.

Table 3
Williams–Landel–Ferry function constants, SMP-aramid composite (SMPC).

Specimens	SMP matrix	0° SMPC	45° SMPC
C1	9.9	55.5	22.7
C2	56.9	384	89.7
T_r	80 °C	50 °C	50 °C

Table 4
SMP-aramid elastic modulus.

Direction	Elastic modulus (MPa)		
	One-layer	Three-layer	Four-layer
0°/90°	13,200	14,200	8400
22.5°	3180	8500	8210
45°	863	8180	8350

made by TA Instruments which is shown in Fig. 2b. Fig. 2(c) shows the placement of the specimen.

DMA measures the complex modulus which comprises the storage E′ and the loss E″ moduli. The storage modulus can be thought of as the energy stored in the elastic part while the loss modulus is the energy dissipated through heat due to friction. A multi-frequency-strain test was carried out with an oscillatory strain of 10 μm applied at frequency range from 0.30 Hz to 32 Hz with a spacing of two points per decade. A constant heating rate of 1 °C/min from 40 °C to 85 °C was applied during each test. Fig. 3 shows the variation of E′, E″ and the ratio $\tan \delta = E''/E'$ obtained from a DMA test carried out at 1 Hz [44]. The tan δ ratio (loss factor) is a measure of the material mechanical damping [45]. The storage modulus was measured from 1340 MPa in the glassy state to 37 MPa in the rubbery state. The loss modulus reached a maximum of 200 MPa during transition from 40 °C to 70 °C. The tan δ ratio, reached a maximum between 60 °C to 70 °C.

This material is suitable to be part of the joint of lightweight structures which are not subjected to heavy loads. For structural applications the 3D printed SMP core requires reinforcement even in the glassy state. For this reason, a reinforcement skin will be discussed in Section 3. The material storage modulus drops significantly from 50 °C. To prevent undesired stiffness reduction, cooling systems are required in hot climate conditions. Alternatively, SMPs with a higher transition temperature may be preferred. Material damping could be improved by means of additions. For example, it has been shown that adding polyamide nonwoven fabrics into a carbon

(a)

(b)
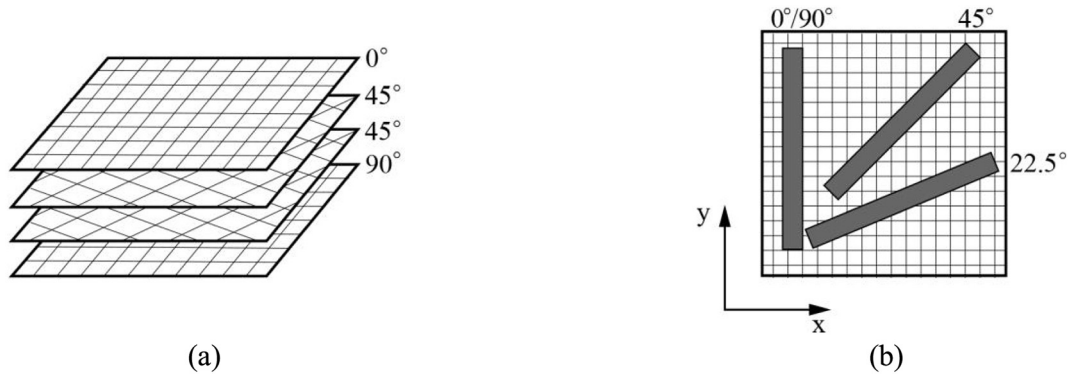
Fig. 7. (a) Four-layer stacking; (b) cutting directions.
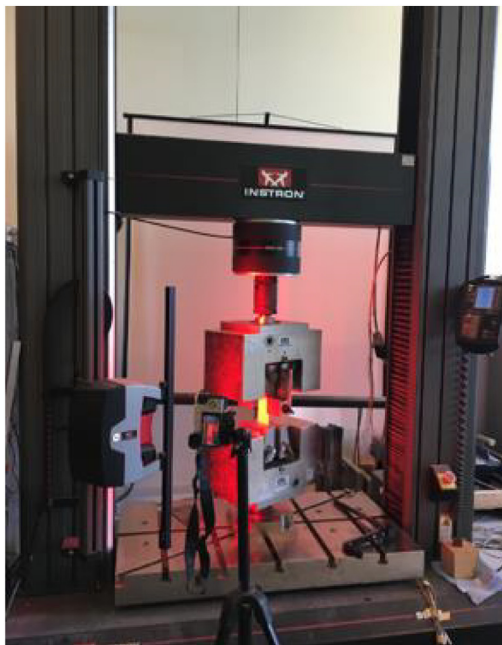
(a)
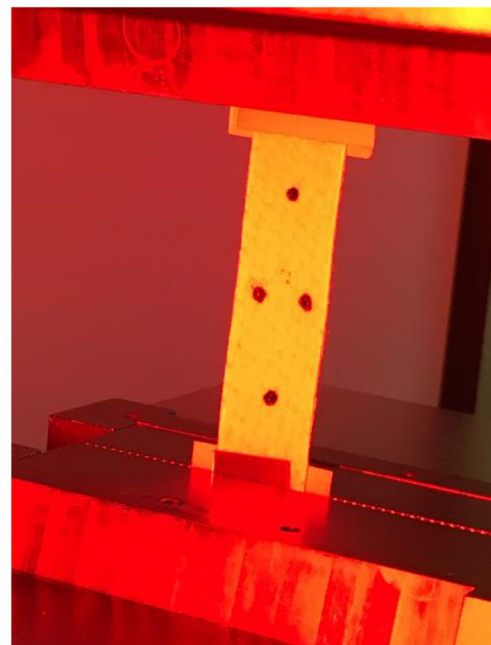
(b)

Fig. 8. (a) Instron tensile tester; (b) SMP-aramid specimen under tension.

Table 5
Measured vs simulated elastic and shear modulus, four-layer SMP-aramid composite.

	Elastic modulus E (MPa)	Shear modulus G (MPa)
Experiment	8320	3150
Simulation	8370	2660

Table 6
Maximum deformation with (d_{rf}) and without (d) reinforcement skin.

	25 °C	40 °C	45 °C	50 °C	55 °C	60 °C	65 °C
d (mm)	152	154	155	158	168	176	187
d_{rf} (mm)	137	139	140	142	149	156	161
Δd (mm)	14.3	15.0	15.2	16.2	18.8	20.1	25.4

fiber reinforced polymer, causes a significant increase of the loss factor tan δ while maintaining the storage modulus unchanged. [46].

2.2. Elastic and viscoelastic material model

For the temperature dependent elastic model (thermoelastic model) only the storage modulus curve at 1 Hz is considered while frequency dependence as well as damping (E″ and tan δ) are neglected. With regard to the viscoelastic model instead, two curves are needed for a full characterization: the shift factor curve and the master curve which are both shown in Fig. 4 for the specimen under testing. The shift factor relates the change

of stress relaxation rate with temperature. The master curve expresses the change of storage modulus over many frequency decades and at different temperatures. In a viscoelastic material, temperature has the effect to speed up the relaxation process without affecting the amount of relaxation. It is therefore common practice to model the storage modulus as:

$$E(t,T) = E(t_{red}, T_{ref}), t_{red} = a_T t, \tag{1}$$

where a_T is the temperature dependent shift factor, t_{red} is the reduced (or shifted) time scale and T_{ref} is an arbitrarily chosen reference temperature.
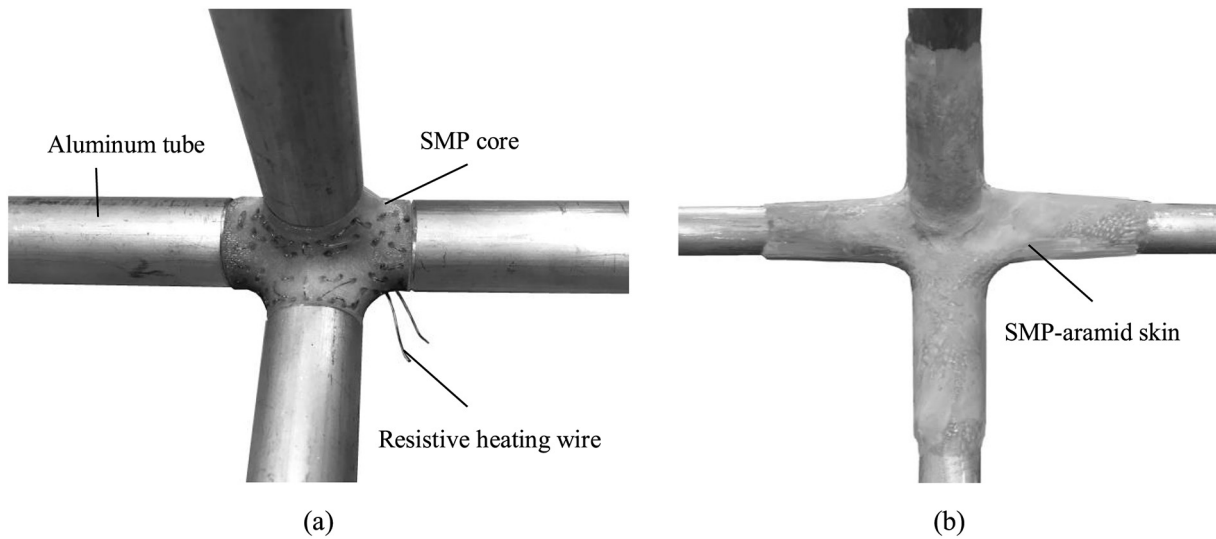
Fig. 9. (a) SMP core connected to four aluminum tubes; (b) SMP-aramid reinforced skin.
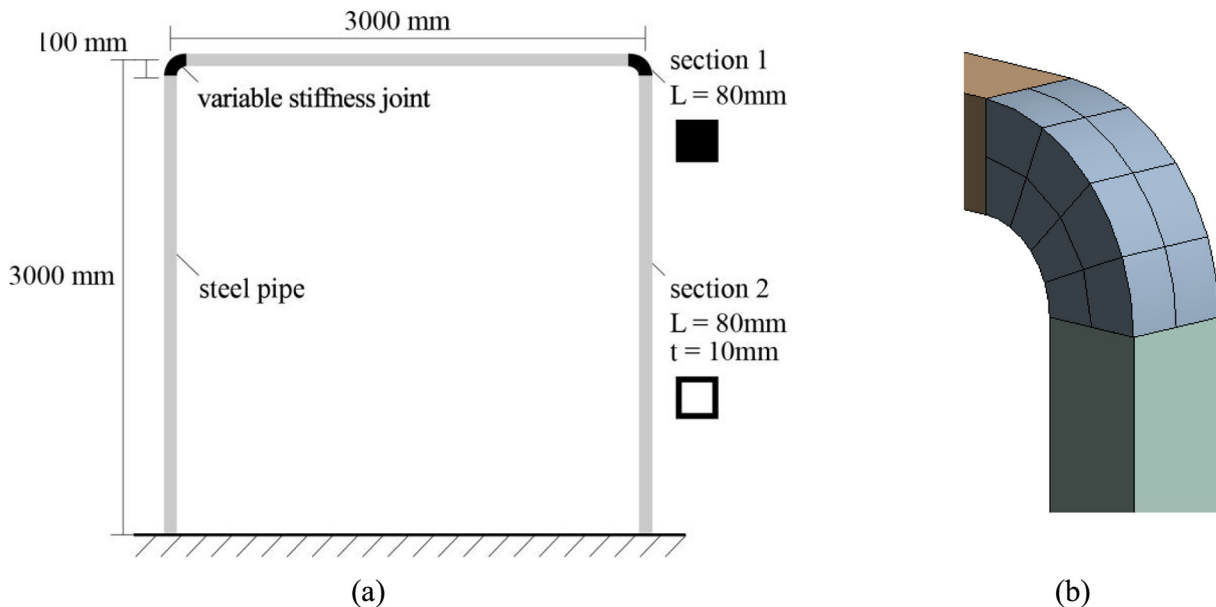
Fig. 10. (a) One-story planar frame equipped with two variable stiffness joints; (b) joint mesh.
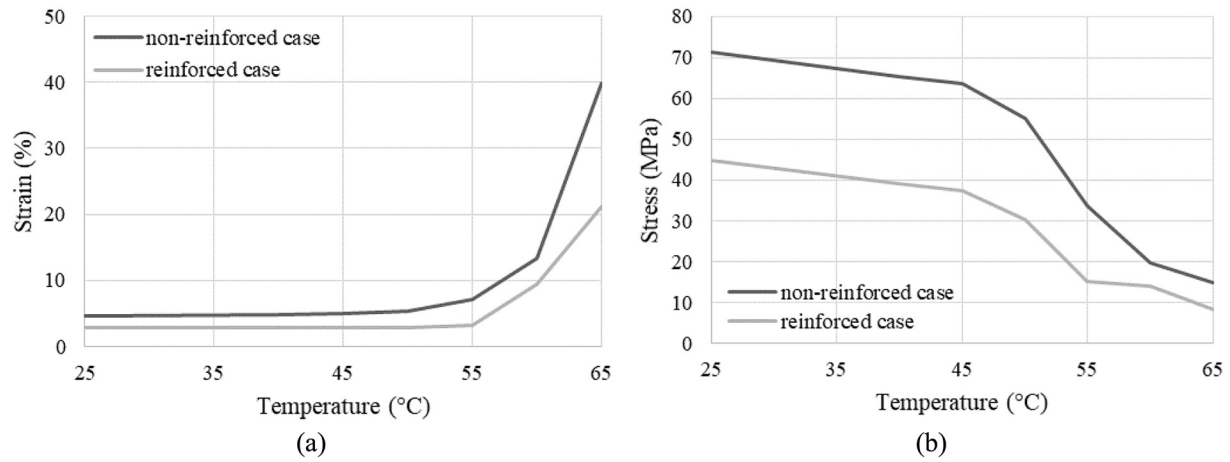
Fig. 11. Equivalent strain (a) and stress (b) (von-Mises) vs temperature for the joint core.

For example, if $a_T = 4$ when the temperature is 10 °C higher than the reference temperature, the stress relaxation will be 4 times faster. Note that in some literature the reduced time is defined as $t_{red} = t/a_T$.

The dashed lines in Fig. 4 bound the storage moduli measured in the frequency range 0.30 Hz to 32 Hz and temperature range 40 °C to 85 °C. At the reference temperature 50°C, which is indicated by square markers, the shift factor is 1. The moduli at a temperature and/or a frequency different to those measured through DMA, are obtained by shifting along the frequency axis using the shift factor curve. The modulus at a higher temperature with respect to the reference temperature is shifted to the left while the modulus at a lower temperature is shifted to the right. For example, at 60 °C the shift factor a_T is approximately 10^4 which means that stress relaxation is faster than that at 50 °C by a factor of 10^4. Consequently, the storage modulus curve at 60 °C, which is indicated by circle markers, shifts by a factor of 10^4 to the left thus forming part of the master curve. The reader is referred to the work of Ferry [43] for more details to obtain a master curve.

In order to efficiently implement master and shift factor curves for numerical simulation, both curves have been approximated though fitting. The master curve is approximated by Prony series for the storage E′ and loss modulus E″:

$$E\prime(\omega) = E_e + \sum_{i=1}^{m} \frac{\omega^2 \rho_i^2 E_i}{\omega^2 \rho_i^2 + 1} \tag{2}$$

$$E''(\omega) = \sum_{i=1}^{m} \frac{\omega \rho_i E_i}{\omega^2 \rho_i^2 + 1} \tag{3}$$

where E_e, E_i and ρ_i are the equilibrium modulus, relaxation strengths, and relaxation times, respectively. The coefficients used in this work are obtained using a non-linear curve fit procedure. The shift factor curve is approximated through the Williams–Landel–Ferry function

(WLF):

$$log(a_T) = \frac{-C_1(T-T_r)}{C_2 + (T-T_r)} \tag{4}$$

The fitting was limited to the temperature range of 40 °C to 85 °C which covered most of the glass transition. The constants C_1 and C_2 are given in Table 1. T_{ref} and T_g are the reference and glass transition temperature, respectively.

3. Design and characterization of the SMP-aramid reinforcement skin

The purpose of the reinforcement skin is to limit the deformation of the SMP core when subjected to loading in its rubbery state. Often structural joints have complex geometries to connect many elements and therefore are subjected to forces of different directions including bending and torsion. For this reason, a reinforcement skin should behave as an isotropic material.

The skin tested in this study was made of an SMP matrix impregnated with an aramid fabric made by *Easy Composites Ltd* (Stoke-on-Trent, UK). This aramid fabric is woven in a satin pattern (3HS) of Kevlar® 49 yarn with a weight of 175 g/m² and a thickness of 0.27 mm. The SMP material of the joint core was not suitable for impregnation of the aramid fabric due to high viscosity. For this reason, a two component SMP resin was employed – MP5510 SMP (potting type) made by *SMP Technologies Inc* (Tokyo, Japan). The resin part (MP-5510A) and hardener (MP-5510B) were mixed with a weight ratio of 2:3. The matrix so obtained was impregnated with the aramid satin weave fabric in a vacuum bag as shown in Fig. 5a. After impregnation, the SMP composite was cured at 70 °C for three hours. To characterize the mechanical properties of this composite, rectangular specimens of dimension 20 mm × 5 mm were cut from the composite at 0°/90° and ± 45° as indicated in the diagram shown in Fig. 5c. For comparison, specimens of identical dimensions were also cut from the SMP matrix (no aramid fabric). The SMP-aramid

Table 7
1st natural frequency vs temperature.

	25 °C	40 °C	45 °C	50 °C	55 °C	60 °C	65 °C
ω (Hz)	5.84	5.79	5.78	5.72	5.57	5.46	5.33
Sω (%)	–	0.76	0.97	2.00	4.56	6.53	8.72
σ (MPa)	0.43	0.38	0.37	0.30	0.15	0.059	0.040
ε (%)	0.030	0.031	0.031	0.031	0.033	0.043	0.11
ω_{rf} (Hz)	6.11	6.07	6.06	6.01	5.88	5.77	5.68
Sω_{rf} (%)	–	0.61	0.77	1.61	3.72	5.49	6.99
σ_{rf} (MPa)	0.38	0.34	0.33	0.27	0.13	0.053	0.024
ε_{rf} (%)	0.027	0.027	0.027	0.028	0.030	0.039	0.073

Table 8
2nd natural frequency vs temperature.

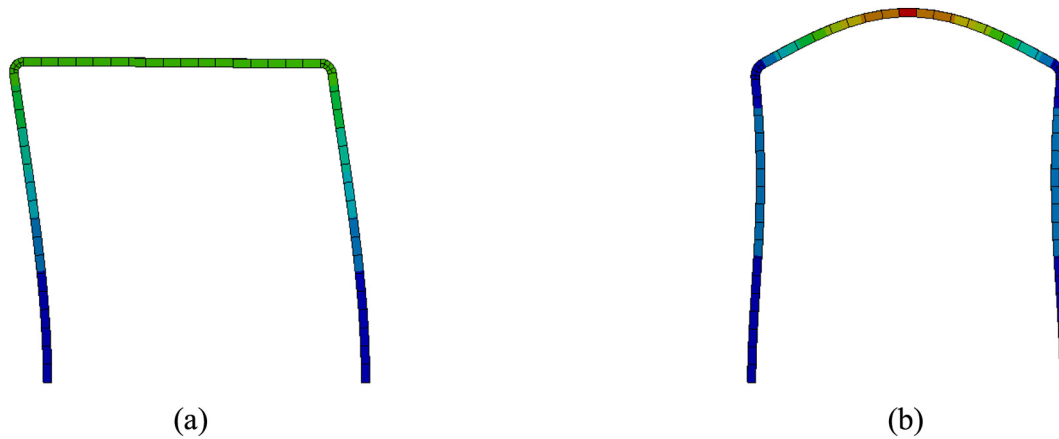|	25 °C	40 °C	45 °C	50 °C	55 °C	60 °C	65 °C
ω (Hz)	27.0	26.9	26.8	26.5	25.4	22.4	16.1
Sω (%)	–	0.64	0.83	1.86	6.11	17.3	40.5
σ (MPa)	1.72	1.59	1.56	1.40	1.07	0.80	0.41
ε (%)	0.12	0.13	0.13	0.15	0.24	0.59	1.15
ω_{rf} (Hz)	27.9	27.8	27.7	27.6	27.1	26.4	25.9
Sω_{rf} (%)	–	0.41	0.53	1.13	2.97	5.17	7.17
σ_{rf} (MPa)	1.42	1.28	1.24	1.06	0.62	0.29	0.13
ε_{rf} (%)	0.099	0.10	0.10	0.11	0.14	0.21	0.38

Fig. 12. (a) 1st modal shape; (b) 2nd modal shape.

specimens were tested at a frequency of 1 Hz, 3 Hz, 10 Hz, 30 Hz and 60 Hz through DMA which was carried out similarly to the test performed for the joint core material.

3.1. SMP-aramid single layer composite

Fig. 6 shows the plot of storage modulus and tan δ as a function of the temperature for the SMP matrix (no aramid fabric). Comparing with Fig. 3, it can be seen that for this type of SMP, the glassy modulus is slightly higher (1780 MPa vs 1340 MPa) and that the glass transition range is somewhat broader (40 °C to 75 °C). The tan δ reaches a maximum at a higher temperature (80 °C versus 68 °C). Similarly, this material also features a drastic reduction of the storage modulus after mild heating.

As predicted, after impregnation of the aramid fabric, the glassy modulus increased drastically along the 0°/90° directions. The glass transition temperature is 5 °C–10 °C higher and the tan δ is lower with respect to the SMP matrix without aramid fabric. For the specimen cut at ±45°, the aramid fibers do not contribute to increase the stiffness. Glassy modulus, glass transition range and tan δ curves are almost identical to that of the matrix material. The storage modulus and tan δ as function of temperature for the SMP-aramid specimens are reported in the Appendix (Figs. A1 and A2).

As expected, the single layer composite features a directional dependency of the stiffness which is high when the load is applied along the 0° and 90° directions aligned with the weft and warp of the aramid fabric while it is low in the ±45° directions. The glassy E_g and rubbery E_r storage moduli, which were measured at T_g - 40 °C and T_g + 40 °C respectively, are given in Table 2.

Master and shift factor curves were obtained for the SMP-aramid material from DMA tests. The curves for the 0°/90° type, ±45° type and SMP matrix are given in the Appendix (Figs. A3, A4, A5). The WLF constants for the shift factor curve are listed in Table 3.

3.2. Design of a quasi-isotropic SMP-aramid skin

To improve the mechanical properties along the ±45° directions, another layer of aramid weave with fibers oriented at ±45°was added. However, a two-layer laminate is not symmetric and it is likely to warp after cooling hence a three and a four-layer stacking were tested. The three-layer laminate had a [0F/45F/0F] stacking sequence where 0F stands for the orthotropic 0°/90° aramid Fabric. The four-layer laminate had a [0F/45F₂/0F] stacking sequence which is shown in Fig. 7(a). Samples for uniaxial tension testing were cut at 0°, 22.5°, and 45° as shown diagrammatically in Fig. 7(b). Tensile testing was carried on a 50 kN Instron which was equipped with a non-contact video extensometer (AVE2) (Fig. 8).

Table 4 gives the elastic modulus measured from the tensile tests. As expected, compared to the one-layer composite, the three-layer one is stiffer in the 45° direction. However, the stiffness is not equally distributed because the composite is made of two 0°/90° plies and only one ± 45° ply. For the four-layer composite, however, the stiffness is almost independent from the direction of loading. The ultimate tensile stress and strain (averaged over the three directions) are 107 MPa and 1.9%, respectively. A Poisson's ratio of 0.32 was obtained through measurements made by the video extensometer.

A model was setup in Ansys Composite PrepPost for validation of the experimental testing. Using the elastic and in-plane shear modulus measured for the one-layer composite, which are 13.6 GPa and 100 MPa respectively, the four-layer stacking sequence was simulated ([0F/45F2/0F]). The measured elastic modulus (Table 4) was in good accordance to that predicted from the model. Table 5 gives the elastic and shear modulus obtained from simulations and experimental testing. The experimental shear stiffness is obtained as G = E/[2(1 + v)] where v is the above mentioned Poisson ratio of 0.32. The shear stiffness obtained from the model is 20% lower than the experimental value. This is likely to be caused by inaccuracies with the determination of the Poisson's ratio through the video extensometer. The transverse strain was very small thus causing relatively large errors. In addition, the imperfect surfaces of the SMP-aramid specimens and the cracks generated during testing might have affected the accuracy of the measurement.

### 3.3. Application of the SMP-aramid reinforcement skin

The variable stiffness joint described in previous sections has been fabricated though fused deposition of the SMP core and manual application of the SMP-aramid skin. Fig. 9(a) shows the SMP core connected to 4 aluminum tubes and (b) the joint after application of the reinforcement skin. This joint is part of a 650 mm × 650 mm × 1325 mm multi-story frame which is currently being tested. Application of the SMP-aramid skin was a challenging task. Due to the complex geometry it was not possible to apply the reinforcement skin uniformly on the joint surface so to cover all areas.

4. Numerical modelling

4.1. One-story planar frame equipped with two variable stiffness joints

The structure considered in this case study is a one-story planar frame equipped with two variable stiffness joints. The structure is shown diagrammatically in Fig. 10(a). The height and width of the frame is 3 m. The supports are fully fixed. The finite element model, implemented in Ansys Workbench, comprises beam elements for the frame and solid elements for the joints. The beam elements are of type BEAM188 and the
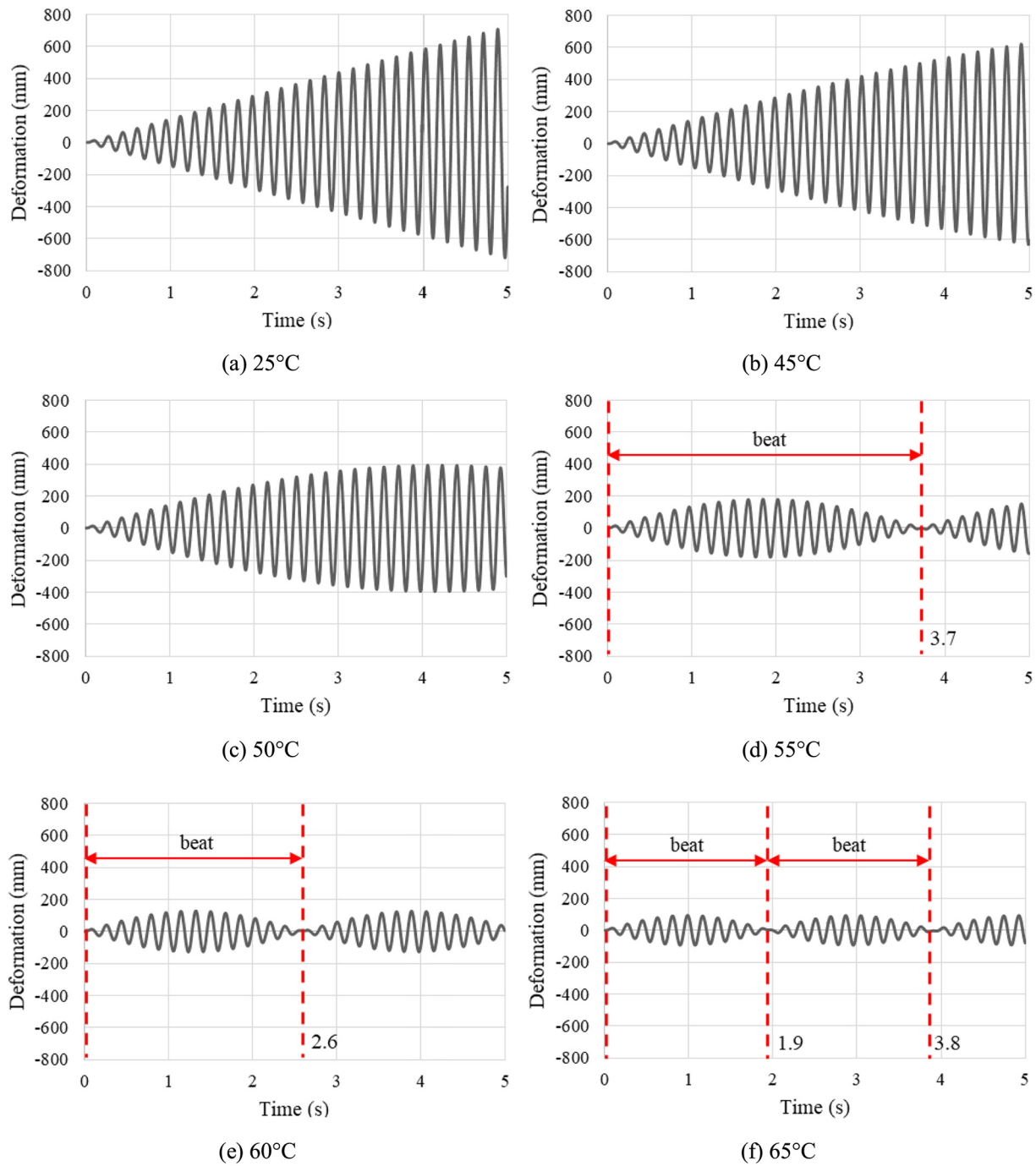
Fig. 13. (a)–(f) Average deformation vs. time at 25 °C, 45 °C, 50 °C, 55 °C, 60 °C and 65 °C; non-reinforced case, elastic material model.

joint elements are of type SOLID186. The beam elements have an 80 mm × 80 mm square hollow section and a wall thickness of 10 mm. Each joint has an 80 mm × 80 mm solid square section; 16 elements are used to mesh each joint. The SMP-aramid skin is modelled using "surface coating" (SURF156) elements. This element is usually employed to apply line pressure loads on structures.

The SMP has been modelled as a variable stiffness purely-elastic material as well as a viscoelastic material. For the elastic material definition, the storage modulus is a function of the temperature but all other viscous effects are ignored. Specifically, the storage modulus measured at 1 Hz (Fig. 3) was chosen for the elastic model. For the viscoelastic material definition, the storage modulus is a function of temperature and deformation frequency. Prony series are employed to approximate the master curve while the shift factor curve is approximated by fitting a WLF function to the measured data (Table 1).

The SMP core will be actuated through resistive heating in a temperature range between 25 °C to 65 °C which is lower than the transition temperature (Table 2). Since the skin is the outer layer, it is reasonable to assume that the SMP matrix of the skin will always be in the glassy state and thus its stiffness is temperature independent. It is expected
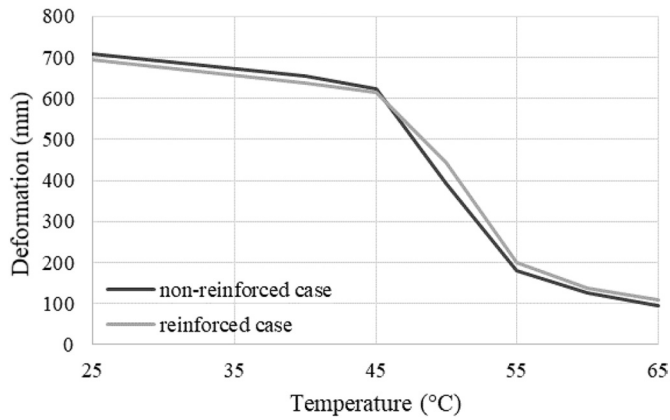
Table 9
'Beat' vs temperature from single degree of freedom reduced model.

	40 °C	45 °C	50 °C	55 °C	60 °C	65 °C
T_b (s)	22.5	17.7	8.5	3.7	2.6	1.9
$T_{b,rf}$ (s)	26.8	21.1	10.2	4.4	2.9	2.3

Fig. 14. Maximum deformation vs joint temperature; non-reinforced vs reinforced case, elastic material model.

Table 10
damping effect for SMP joints vs. reinforced SMP joints.

T (°C)	25 °C	40 °C	45 °C	50 °C	55 °C	60 °C	65 °C
ζ_e (%)	–	0.019	0.038	0.29	0.98	1.18	1.21
ζ_{rf} (%)	–	0.017	0.032	0.22	0.68	0.87	1.16

that the application of the SMP-aramid skin will reduce the joint deformation when in the activated state (i.e. close to the transition temperature) compared to the non-reinforced case. However, it is also expected that the SMP-aramid skin will reduce viscoelastic damping. For this reason, simulations are carried out with and without SMP-aramid skin applied to the joints.

4.2. Static analysis

A linearly distributed load q of 15kN/m is applied to the left column and the top beam. A linear static analysis is carried out with the joints actuated within temperature range 25 °C to 65 °C. Table 6 compares the static deformation of the frame with and without reinforcement skin. As expected, the deformation d when the joints are not reinforced is always larger than the deformation d_{rf} when the joints are reinforced. The difference $\Delta d = d - d_{rf}$ increases as the temperature increases, thus indicating that the SMP-aramid skin is effective to reduce the deformation when the joints are activated closer to the glass transition temperature.

Fig. 11 shows the plot of the equivalent (von-Mises) stress (a) and strain (b) as a function of the actuation temperature for both the non-reinforced and reinforced case. As expected, stress and strain are higher over the whole temperature range for the non-reinforced case. When the joint is heated up to 65 °C, the strain is reduced by approximately 20% for the reinforced case.

4.3. Modal analysis

Modal analysis is carried out to evaluate the effect of joint stiffness variation on the 1st and 2nd natural frequency of the structure when the joints are actuated from ambient to transition temperature (25 °C to
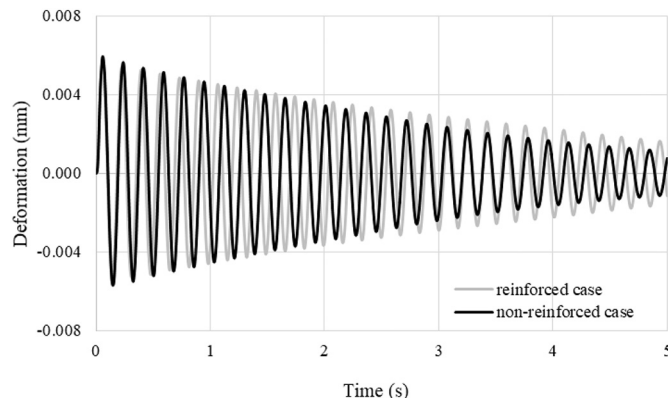

Fig. 15. Average deformation vs time at 55 °C.

65 °C). The natural frequency is indicated by ω_{rf} when the joint is reinforced with the SMP-aramid skin, and by ω for the non-reinforced case.

Table 7 and Table 8 give the variation of the 1st and 2nd natural frequency with the temperature as well as the shift computed against the frequency at ambient temperature, i.e. before joint actuation. The frequency shift is indicated by $S\omega$ and $S\omega_{rf}$ for the non-reinforced and reinforced case respectively. The tables also give the variation of the average stress and strain in the joint with the temperature. As the temperature increases, both 1st and 2nd natural frequency reduce substantially. At the transition temperature the 1st natural frequency reduces by 8.7% and 7.0% for the non-reinforced and reinforced case respectively. As expected, when the SMP-aramid skin is applied to the joint, the structure natural frequency reduces to a lesser degree as the temperature increases towards the transition one.

This effect is substantial for the 2nd mode. The 2nd natural frequency reduces by 40.5% and 7.2% for the non-reinforced and reinforced case respectively. Compared to the 1st modal shape, the 2nd modal shape causes a larger deformation in the joint core.

For the non-reinforced case, the average strain in the joint core at 25 °C for the 1st and 2nd mode is 0.030% and 0.12%, and the average stress is 0.43 MPa and 1.72 MPa, respectively. At 65 °C, the average strain increases to 0.11% and 1.15% while the average stress decreases to 0.040 MPa and 0.41 MPa for the 1st and 2nd mode respectively. The reinforced skin limits the joint deformation drastically. For the reinforced case, the average strain in the joint core at 25 °C for the 1st and 2nd mode is 0.027% and 0.099%, and the average stress is 0.38 MPa and 1.42 MPa, respectively. At 65 °C, the average strain increases to 0.073% and 0.38% while the average stress reduces to 0.024 MPa and 0.13 MPa for the 1st and 2nd mode respectively. The increase of strain due to heating is much lower for the 2nd mode in the reinforced case (280%) compared to the non-reinforced case (850%). Similar considerations apply to the decrease of stress in the joint which is much larger for the reinforced case (91%) compared to the non-reinforced case (76%). This is because the reinforcement skin takes most of the deformation. This results in a larger frequency shift in the non-reinforced joint for the 2nd mode with respect to the non-reinforced case. The 1st and 2nd modal shapes are shown in Fig. 12.

4.4. Mode superposition transient dynamic analysis

In this section, transient analysis is carried out to evaluate whether the frequency shift obtained through joint stiffness variation is effective to reduce the structure dynamic response. A linearly distributed sinusoidal load $q_s = A \sin (2\pi\omega_r t)$ with amplitude A = 1kN/m is applied to the left column of the frame in order to excite the 1st mode. The load frequency is identical to the fundamental frequency which is 5.84 Hz for the non-reinforced case and 6.11 Hz for the reinforced case at $T = 25$ °C. In this study, transient analysis is carried out through mode-superposition. This implies that the joint core (SMP) is modelled as a thermo-elastic material. This is because mode-superposition is a linear structural dynamic analysis method and thus a viscoelastic material definition is not possible.

Fig. 13 shows the plot of the structure average deformation vs time for the non-reinforced joints before actuation (T = 25 °C) and when the joint is actuated close to the transition temperature (range 45 °C to 65 °C). Without joint stiffness variation (25 °C), the deformation increases steadily with time because of resonance. Through joint stiffness variation instead, the dynamic response reduces substantially. From
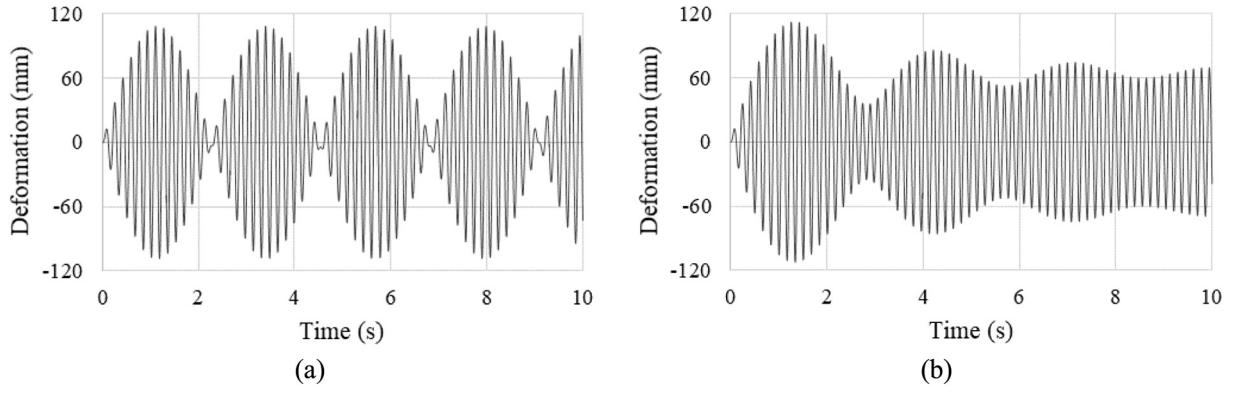
Fig. 16. Average deformation vs time for elastic (a) and viscoelastic (b) case; $T = 65$ °C.

$T = 50$ °C resonance is avoided in less than 5 s. The average deformation decreases from 700 mm at 25 °C to less than 100 mm at 65 °C.

If the frame is reduced to a single degree of freedom structure, assuming a zero initial displacement and velocity, the deformation as a function of time can be estimated as:

$$u(t) = \frac{p_0}{k} \frac{1}{1 - \left(\frac{\omega_e}{\omega}\right)^2} \left(\sin\omega_e t - \frac{\omega_e}{\omega} \sin\omega t \right) \qquad (5)$$

In Eq. (5) p_0/k is the maximum static deformation caused by the applied load, ω_e and ω are the excitation and natural frequency respectively. This model has been employed to verify the findings obtained through transient analysis. From the reduced model, it is simple to compute the single cyclic pulsation of $u(t)$ – the so called "*beat*". The frequency of the beat is $\omega_b = |\omega - \omega_e|$ and its period is $T_b = 1/\omega_b$ [47]. The variation of T_b with the temperature computed for the reduced model is given in

Table 9. For comparison, the beat periods are also indicated by dashed lines in Fig. 13. Comparison with simulation results show very good accordance.

Similar results are obtained when the joint is reinforced with the SMP-aramid skin (Fig. A6). Also in this case the average deformation decreases as the temperature increases. However, for a temperature above 55 °C, the deformation amplitude reduces less for the reinforced case due to a smaller frequency shift compared to the non-reinforced case.

Fig. 14 compares the maximum deformation component in the x-axis over a period of 5 s. For both non-reinforced and reinforced case, the deformation decreases substantially as the joint stiffness decreases. In both cases, the deformation reduces very rapidly between $T = 45$ °C and $T = 55$ °C. In both cases, the frequency shifts at 55 °C (4.56% and 3.72% for the non-reinforced and the reinforced case respectively) cause a significant reduction of the deformation from approximately 700 mm to 200 mm. For this reason, the target actuation temperature is set to 55 °C which is 10 °C lower than the glass transition temperature.
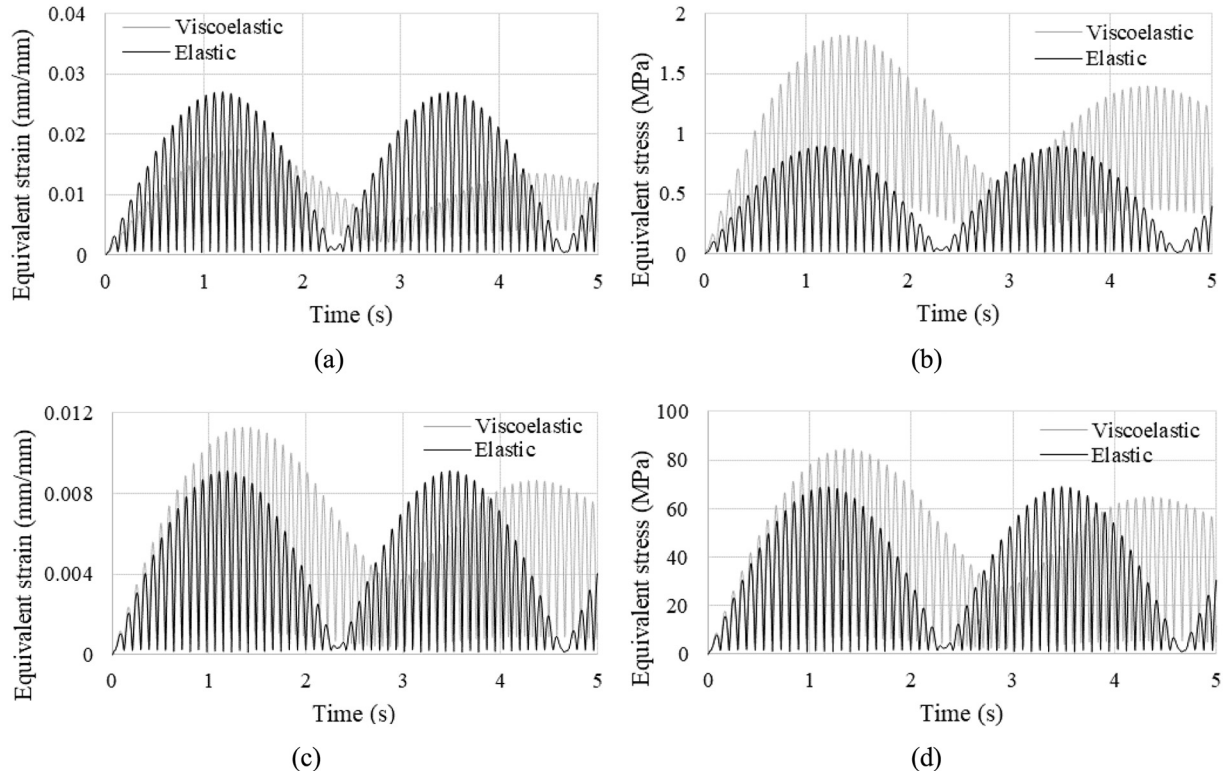

Fig. 17. (a) Strain and (b) stress vs time, SMP core; (c) strain and (d) stress vs time, SMP-aramid skin; T = 65 °C.
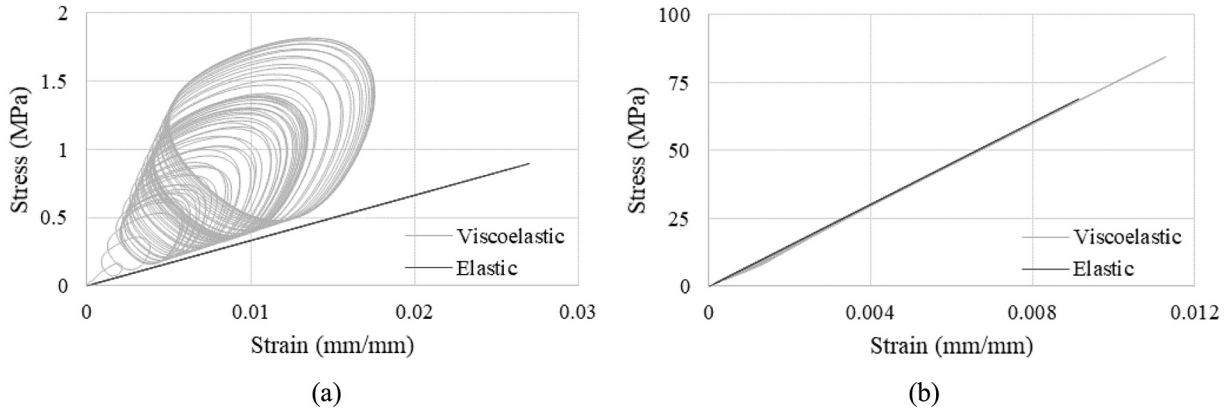
Fig. 18. (a) Stress vs strain SMP core; (b) Stress vs strain SMP-aramid skin.

4.5. Non-linear transient dynamic analysis

In the simulation carried out so far, the SMP has been treated as an elastic material with a temperature dependent modulus. Material stiffness is dependent on the temperature but time and strain rate dependency are neglected. This greatly simplifies transient analysis which can be carried out though mode superposition. However, this way it is not possible to model damping and energy dissipation caused by viscoelasticity which is the subject of this section.

4.5.1. Dynamic analysis with a viscoelastic material model

An identical set of simulations to that described in Section 4.4 has been carried out through non-linear transient dynamic analysis using a viscoelastic material model. For brevity, only the reinforced case is considered. Similar results are obtained compared to the elastic material model for the reinforced case. As before, actuation of the joints through resistive heating is effective to cause a significant shift of the natural frequency under resonance loading. The average deformation of the structure reduces substantially from 684 mm at ambient temperature to 211 mm when the joint core temperature reaches 55 °C. For brevity, the plots of the structure average deformation as a function of time over the considered temperature range (25 °C to 65 °C) and that of the maximum deformation component along the x-axis over a period of 5 s for the elastic and viscoelastic material model, are given in Appendix (Fig. A7). Simulation results confirm that a simplified model which considers SMP as an elastic material with a temperature dependent modulus is acceptable to quantify the structure deformation reduction caused by the frequency shift (Fig. A8).

4.5.2. Damping and energy dissipation

The structure free vibration is simulated to quantify damping effects caused by the viscoelastic joints. A 1 N/m impulse load is applied to the left column of the frame. The plot of the free vibration obtained from non-linear transient analysis is shown in Fig. 15 for both non-reinforced and reinforced case. Note that no global damping coefficient is set. The deformation decay rate is emergent due to the viscoelastic effect.

The damping ratio ζ can be computed from the logarithmic decrement $\Delta = \ln(u_t/u_{t+1})$ as:

$$\zeta = \frac{\Delta/2\pi}{\sqrt{1 + (\Delta/2\pi)^2}} \quad (6)$$

Table 10 gives the damping ratio at different temperatures for non-reinforced ζ_e and reinforced case ζ_{rf}. As expected, since the SMP-aramid reinforcement skin reduces the joint deformation, generally the damping effect is also reduced with respect to the non-reinforced case. However, this effect is small. The damping decreases by a maximum of 30% with respect to the non-reinforced case at 55 °C. As observed in Section 4.5.1, at 55 °C the deformation is drastically reduced in either cases.

4.5.3. Joint behavior: elastic vs. viscoelastic

The mechanical behavior of the joint reinforced by the SMP-aramid skin is taken under analysis in this section. Comparison between elastic and viscoelastic material model is carried out when the joint is heated to the transition temperature of 65 °C. The structure is subjected to the same resonance loading q_s (to excite the 1st mode) defined in Section 4.4. The plot of the average deformation component in the x-axis over a period of 10s as a function of the temperature for elastic and viscoelastic cases are shown in Fig. 16(a) and (b) respectively. Note that the average deformation for the viscoelastic case always lags behind with respect to the elastic case because of the damping effect caused by viscoelasticity. The beats of the viscoelastic case are damped out gradually while the peaks of the elastic beats are constant over several periods.

The plot of the average strain and stress as a function of time for the joint core and skin are shown in Fig. 17. As for the average deformation, the strain and stress for the viscoelastic case always lag behind with respect to the elastic case. The same applies to the beats of the average strain and stress for the viscoelastic case which are damped out gradually over several periods. The stress for the viscoelastic case is higher with respect to elastic case. Since a frequency independent modulus at 1 Hz was chosen for the elastic model, at higher deformation frequencies the viscoelastic material responds with a higher modulus (i.e. higher stresses). However, over several periods, both stress and deformation for the viscoelastic case are damped out and eventually they reduce below those of the elastic case.

Fig. 18(a) shows the plot of the stress vs strain for the SMP core in the elastic and viscoelastic case. In the elastic case the stress varies linearly with the strain. The modulus (the slope in Fig. 18(a)) is approximately 33.2 MPa, which is close to the experimental value of 39 MPa. The strain varies between 0 and 3% whereas the stress between 0 and 0.9 MPa. For the viscoelastic case instead, the strain and stress are out of phase. In this case, the stress vs. strain graph is a hysteresis curve showing the energy dissipated due to damping. The SMP-aramid skin is modelled as an elastic material and therefore the strain-stress curve is linear in the elastic a well as viscoelastic case as shown in Fig. 18(b). The modulus of the skin material obtained through this simulation is approximately 7500 MPa for both cases, which is close to the experimental value 8320 MPa.

5. Conclusion

This paper has presented the design and characterization of a variable stiffness structural joint which comprises a 3D printed shape memory polymer core (SMP) and an SMP-aramid composite skin. The viscoelastic

material behavior of the core was measured through Dynamic Mechanical Analysis and it was modelled using Prony series. The reinforcement skin has been applied to limit the joint deformation in the activated state and consists of oriented aramid fiber mats which have been impregnated within an SMP matrix. The reinforcement skin has been designed to be quasi isotropic. Dynamic mechanical simulations showed that the skin layer mainly features elastic behavior.

The joint stiffness reduces through resistive heating. This effect has been investigated as a control strategy to reduce the dynamic response of a planar frame structure under resonance loading. The frame is assumed to be equipped with two variable stiffness joints. Numerical simulations have shown that the joint stiffness reduction is able to cause a significant shift of the structure natural frequencies which results in a substantial decrease up to 84% of the maximum displacement under resonance loading. The shift of the fundamental frequency is 8.7% and 7.0% for the non-reinforced and reinforced case respectively when the joint is actuated to the transition temperature of 65 °C. However, even when the joints are actuated to a lower temperature of 55 °C the frequency shift is sufficient to avoid resonance. The application of a reinforcement skin has reduced the deformation without significantly affecting the frequency shift caused by the joint stiffness variation. The reinforcement skin is effective to limit the joint deformation while having only a limited effect on the damping caused by the viscoelastic behavior of the core material. The damping decreases by a maximum of 30% when the joint is actuated to 55 °C with respect to the non-reinforced case. However,

vibration reduction is primarily caused by the frequency shift and thus is not substantially affected.

This paper has shown that the integration of variable stiffness joints in planar reticular structures could be an effective way to control the dynamic response. Control time delay due to heating and cooling, as well as fatigue have not been considered in this work. Future work involves other studies including the effect of control time delay and fatigue as well as simulation and experimental testing on spatial structures with complex layout in order to generalize the conclusions reached in this work.

Declaration of competing interest

The authors declare that they have no known competing financial interests or personal relationships that could have appeared to influence the work reported in this paper.

Acknowledgements

Data availability

The raw and processed data required to reproduce these results are available by contacting the authors.
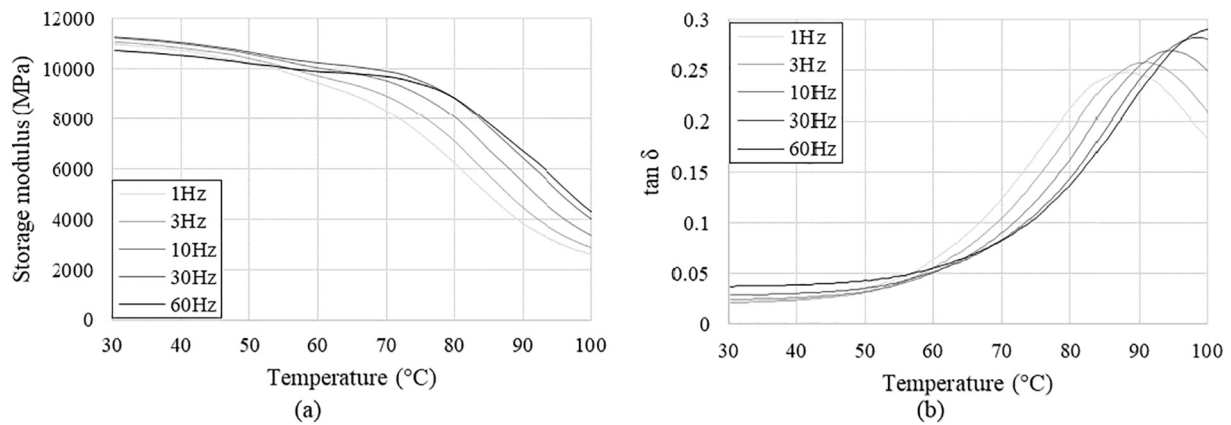
Appendix A

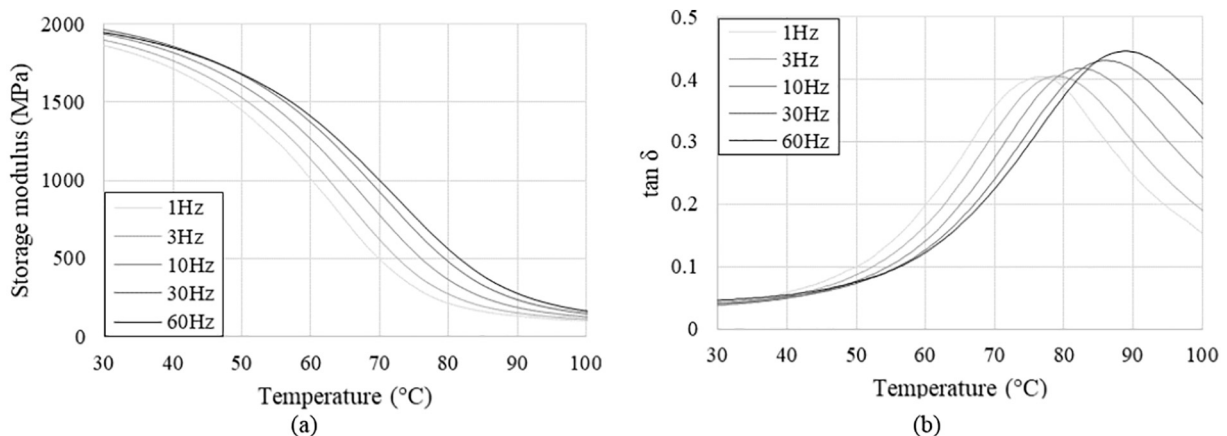**Fig. A1.** (a) Storage modulus and (b) tan δ, SMP-aramid 0°/90° specimen

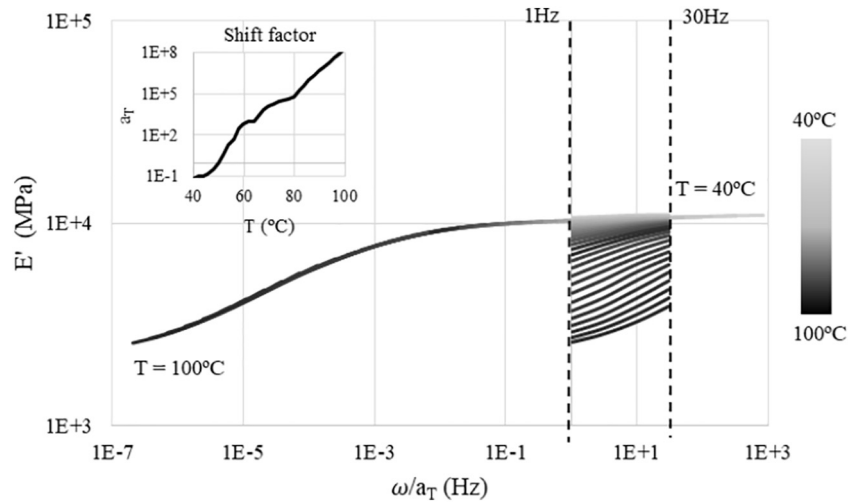**Fig. A2.** (a) Storage modulus and (b) tan δ, SMP-aramid ±45° specimen.

Fig. A3. Master and shift factor curves, SMP-aramid 0°/90° specimen ($T_{ref} = 50$ ° C).

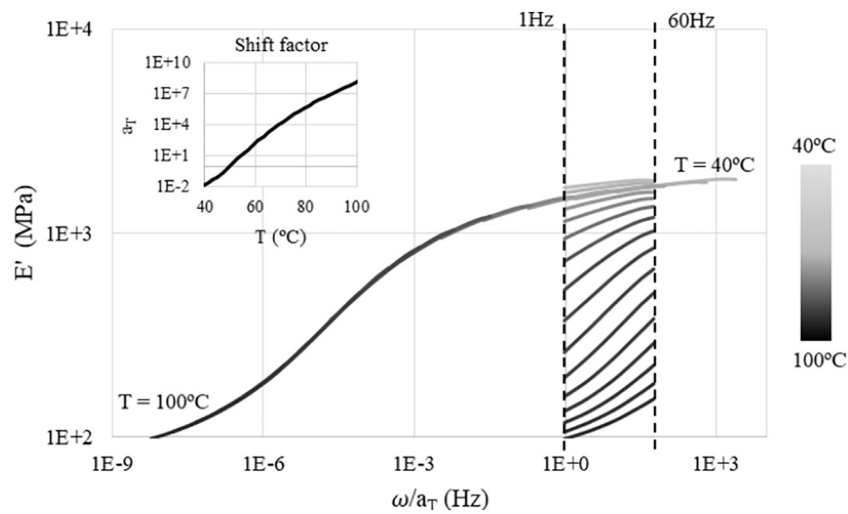**Fig. A4.** Master and shift factor curves, SMP-aramid ±45° specimen ($T_{ref} = 50$ ° C).

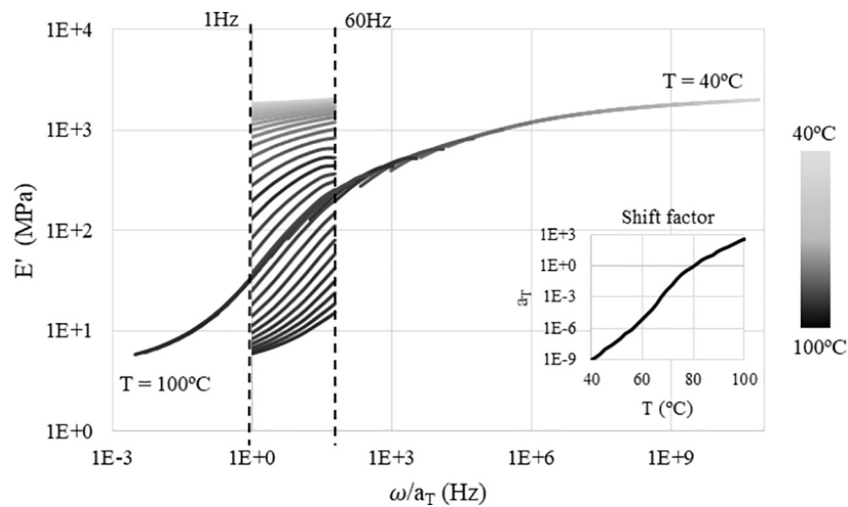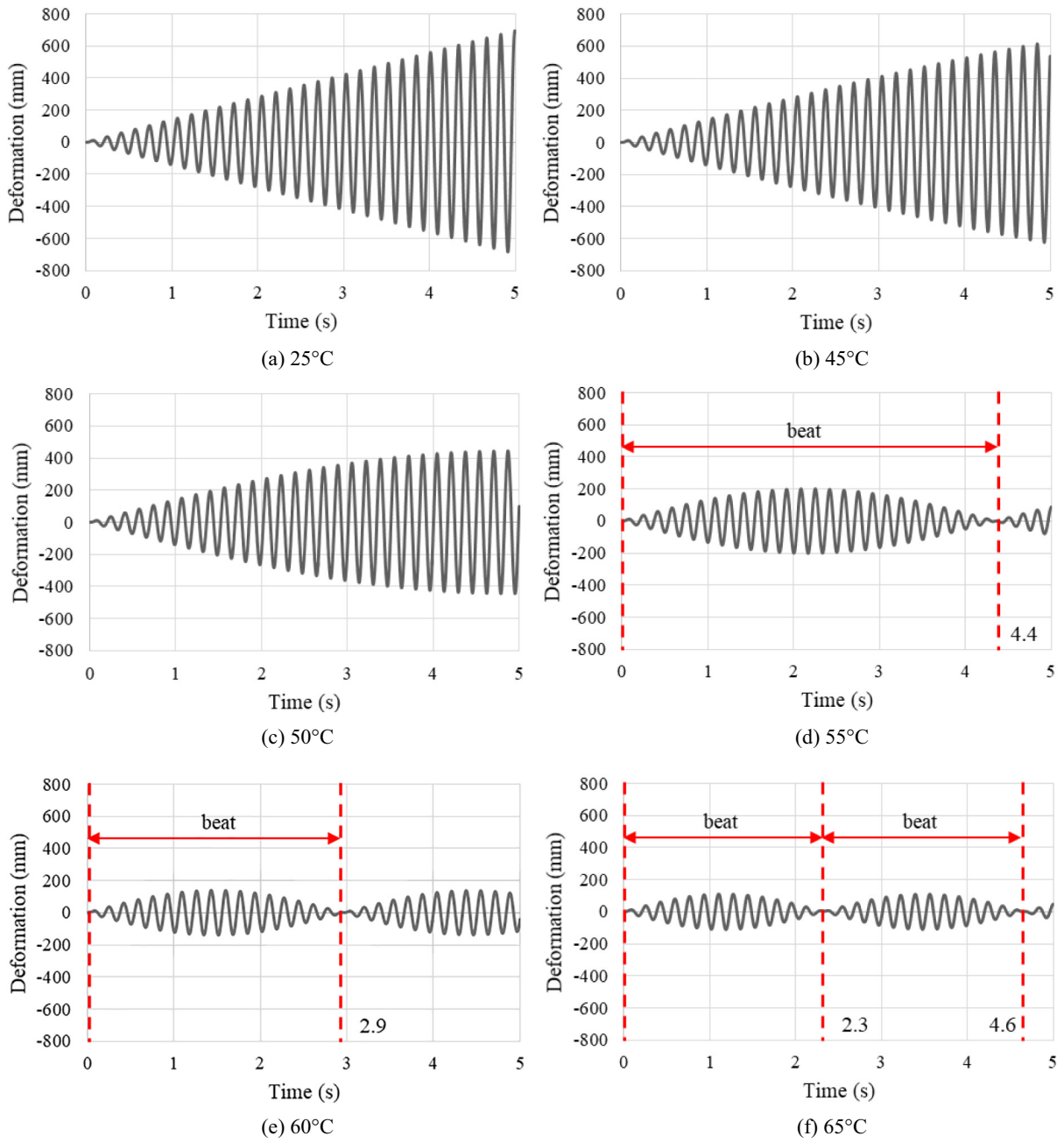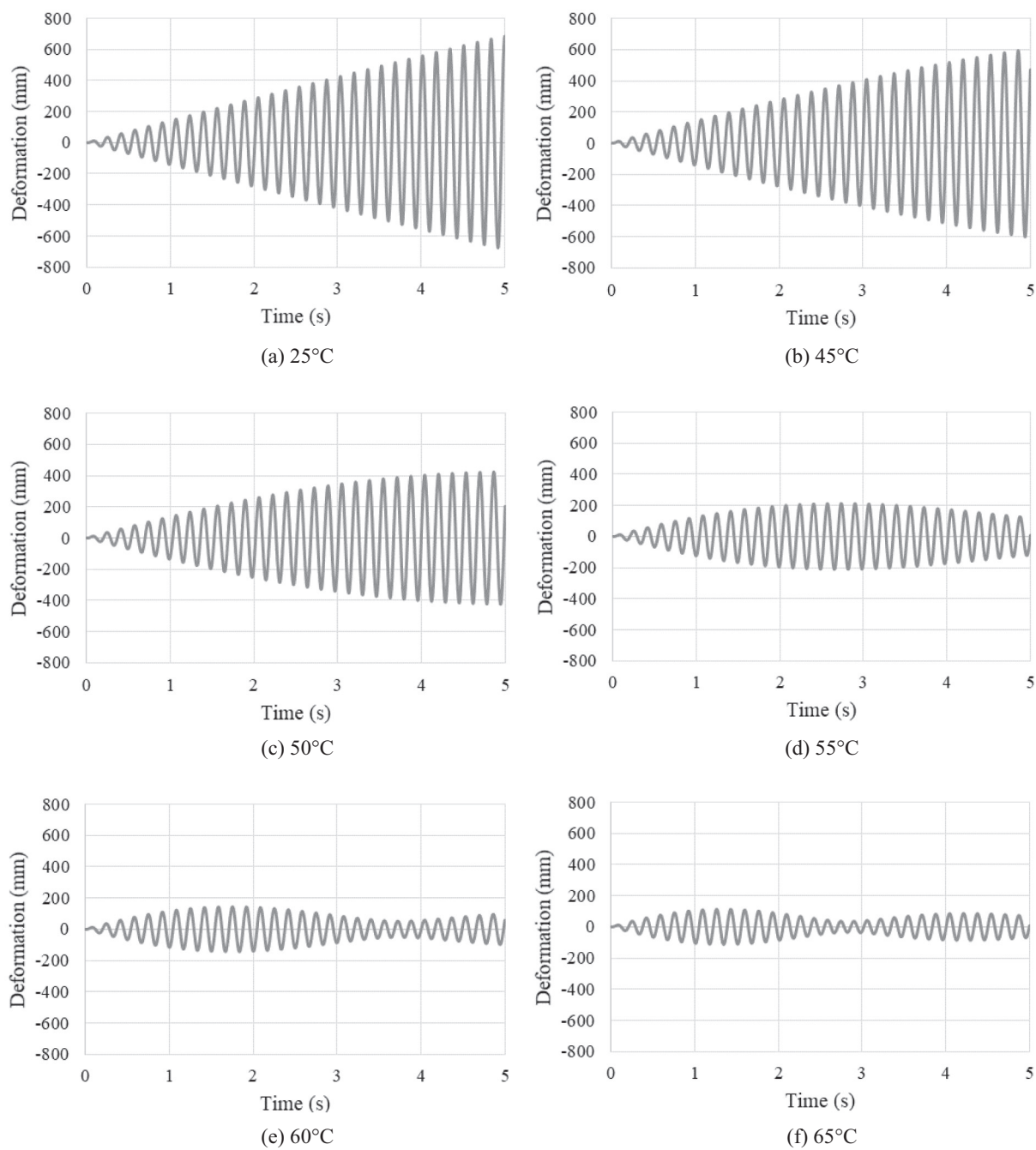**Fig. A5.** Master and shift factor curves, SMP matrix without aramid fabric($T_{ref} = 80$ ° C).

Fig. A6. (a)–(f) Average deformation vs. time at 25 °C, 45 °C, 50 °C, 55 °C, 60 °C and 65 °C; reinforced case, elastic material model.

Fig. A7. (a)–(f) Deformation vs. time at 25 °C, 45 °C, 50 °C, 55 °C, 60 °C and 65 °C; reinforced case, viscoelastic material model.
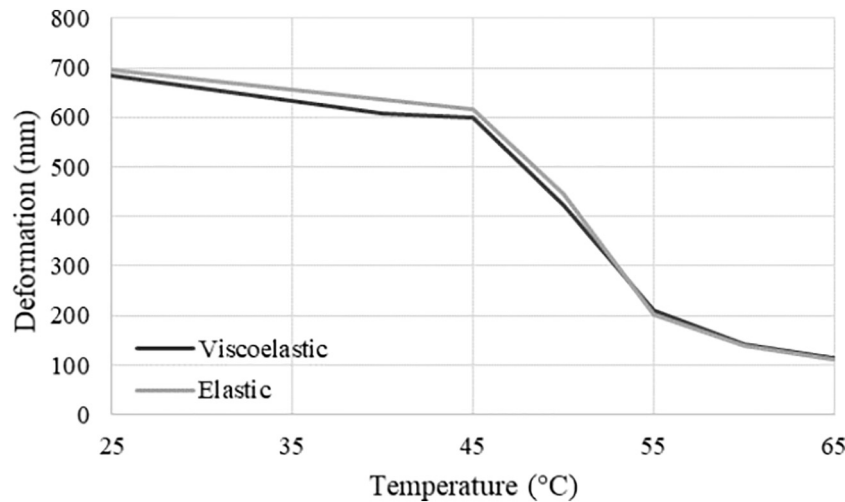
Fig. A8. Maximum deformation vs temperature; reinforced case, elastic vs viscoelastic material model

Appendix B. Supplementary data

Supplementary data to this article can be found online at https://doi.org/10.1016/j.matdes.2019.108353.

References

[1] A. Preumont, K. Seto, Active Control of Structures, John Wiley & Sons, 2008.
[2] T.T. Soong, B.F. Spencer, Active, semi-active and hybrid control of structures, Bull. N. Z. Soc. Earthq. Eng. 33 (3) (2000) 387–402.
[3] B.F. Spencer Jr., R.E. Christenson, S.J. Dyke, Next generation benchmark control problem for seismically excited buildings, Proceedings of the Second World Conference on Structural Control, 1998 , Kyoto.
[4] Y. Ohtori, R.E. Christenson, B.F. Spencer Jr., S.J. Dyke, Benchmark control problems for seismically excited nonlinear buildings, J. Eng. Mech. 130 (4) (2004) 366–385.
[5] J.N. Yang, A.K. Agrawal, B. Samali, J.-C. Wu, Benchmark problem for response control of wind-excited tall buildings, J. Eng. Mech. 130 (4) (2004) 437–446.
[6] G. Kınay, G. Turan, A hybrid control of seismic response by passive and semi-active control strategies, Journal of Engineering Science and Design 2 (1) (2012) 27–36.
[7] T.T. Soong, State of the art review: active structural control in civil engineering, Eng. Struct. 10 (1988) 74–84.
[8] T.T. Soong, J.C.H. Chang, Active vibration control of large flexible structures, Shock Vib. Bull 52 (1982) 47–54.
[9] B. Xu, S. Wu, K. Yokoyama, Neural networks for decentralized control of cable-stayed bridge, Journal of Bridge Engineering (ASCE) 8 (2003) 229–236.
[10] A. Reinhorn, T.R.M. Soong, R. Lin, Full-scale implementation of active control. II: installation and performance, J. Struct. Eng. 119 (6) (1993) 1935–1960.
[11] S.F. Mirfakhraei, G. Andalib, R. Chan, Numerical investigation on toggled actuator forces in active vibration control system, Advance Researches in Civil Engineering 1 (2) (2019) 16–35.
[12] Y.-L. Zhao, Z.-D. Xu, W. Cheng, Wind vibration control of stay cables using magnetorheological dampers under optimal equivalent control algorithm, J. Sound Vib. 443 (2019) 732–747.
[13] M.D. Symans, M.C. Constantinou, Semi-active control systems for seismic protection of structures: a state-of-the-art review, Eng. Struct. 21 (6) (1999) 469–487.
[14] B.F. Spencer, M.K. Sain, Controlling buildings: a new frontier in feedback, IEEE Control. Syst. Mag. 17 (6) (1997) 19–35.
[15] G. Senatore, P. Duffour, P. Winslow, Synthesis of minimum energy adaptive structures, Struct. Multidiscip. Optim. (2019) https://doi.org/10.1007/s00158-019-02224-8.
[16] G. Senatore, P. Duffour, P. Winslow, Energy and cost assessment of adaptive structures: case studies, J. Struct. Eng. 144 (8) (2018), 04018107.
[17] G. Senatore, P. Duffour, P. Winslow, Exploring the application domain of adaptive structures, Eng. Struct. 167 (2018) 608–628.
[18] G. Senatore, P. Duffour, P. Winslow, C. Wise, Shape control and whole-life energy assessment of an "infinitely stiff" prototype adaptive structure, Smart Mater. Struct. 27 (1) (2018), 015022.
[19] A.P. Reksowardojo, G. Senatore, I.F.C. Smith, Actuator layout optimization for adaptive structures performing large shape changes, in: I.F.C. Smith, B. Domer (Eds.), Advanced Computing Strategies for Engineering. EG-ICE 2018. Lecture Notes in Computer Science, vol 10864, Lausanne, Springer, Cham 2018, pp. 111–129.
[20] A.P. Reksowardojo, G. Senatore, I.F.C. Smith, Experimental testing of a small-scale truss beam that adapts to loads through large shape changes, Frontiers in Structural Sensing, 93, 2019, p. 5, https://doi.org/10.3389/fbuil.2019.00093.
[21] F.A. dos Santos, A. Rodrigues, A. Micheletti, Design and experimental testing of an adaptive shape-morphing tensegrity structure, with frequency self-tuning capabilities, using shape-memory alloys, Smart Mater. Struct. 24 (2015) 1–10.

[22] N. Bel Hadj Ali, I.F.C. Smith, Dynamic behavior and vibration control of a tensegrity structure, Int. J. Solids Struct. 47 (9) (2010) 1285–1296.
[23] F.A. dos Santos, C. Cismaşiu, Adaptive underslung beam using shape-memory alloys for frequency-tuning, J. Intell. Mater. Syst. Struct. 28 (10) (2017) 1260–1271.
[24] S. Barbarino, O. Bilgen, R. Ajaj, M.I. Friswell, D.J. Inman, A review of morphing aircraft, J. Intell. Mater. Syst. Struct. 22 (9) (2011) 823–877.
[25] G. Senatore, Q. Wang, H. Bier, P.M. Teuffel, The use of variable stiffness joints in adaptive structures, IASS 2017, 2017 , Hamburg.
[26] Q. Wang, G. Senatore, V. Kaymenaki, A. Habraken, P.M. Teuffel, A vibration control strategy using variable stiffness joints, IASS 2018, 2018 , Boston.
[27] J. Leng, X. Lan, Y. Liu, S. Du, Shape-memory polymers and their composites: stimulus methods and applications, Prog. Mater. Sci. 56 (7) (2011) 1077–1135.
[28] Q. Meng, H. Jinlian, A review of shape memory polymer composites and blends, Compos. Part A 40 (2009) 1661–1672.
[29] W.M. Huang, B. Yang, Y.Q. Fu, Polyurethane Shape Memory Polymers, CRC Press, 2011.
[30] M. Cabanlit, D. Maitland, T. Wilson, S. Simon, T. Wun, M.E. Gershwin, J. Van de Water, Polyurethane shape-memory polymers demonstrate functional biocompatibility in vitro, Macromol. Biosci. 7 (1) (2007) 48–55.
[31] W.M. Huang, B. Yang, Y. Zhao, Z. Ding, Thermo-moisture responsive polyurethane shape-memory polymer and composites: a review, J. Mater. Chem. 20 (17) (2010) 3367–3381.
[32] Y.Y.C. Choong, S. Maleksaeedi, H. Eng, J. Wei, P.C. Su, 4D printing of high performance shape memory polymer using stereolithography, Mater. Des. 126 (2017) 219–225.
[33] Y. Zhou, W.M. Huang, Shape memory effect in polymeric materials: mechanisms and optimization, Procedia IUTAM 12 (2015) 83–92.
[34] H. Tobushi, H. Hara, E. Yamada, S. Hayashi, Thermomechanical properties in a thin film of shape memory polymer of polyurethane series, Smart Mater. Struct. 5 (4) (1996) 483.
[35] J. Diani, L. Yiping, G. Ken, Finite strain 3D thermoviscoelastic constitutive model for shape memory polymers, Polym. Eng. Sci. 46 (4) (2006) 486–492.
[36] J. Hu, W. Chen, P. Fan, J. Gao, G. Fang, Z. Cao, F. Peng, Uniaxial tensile tests and dynamic mechanical analysis of satin weave reinforced epoxy shape memory polymer composite, Polym. Test. 64 (2017) 235–241.
[37] Y. Liu, H. Du, L. Liu, J. Leng, Shape memory polymers and their composites in aerospace applications: a review, Prog. Mater. Sci. 56 (7) (2011) 1077–1135.
[38] C. Lelieveld, K. Jansen, P.M. Teuffel, Mechanical characterization of a shape morphing smart composite with embedded shape memory alloys in a shape memory polymer matrix, J. Intell. Mater. Syst. Struct. 27 (15) (2016) 2038–2048.
[39] H. Meng, G. Li, A review of stimuli-responsive shape memory polymer composites, Polymer 54 (9) (2013) 2199–2221.
[40] T. Ohki, Q.Q. Ni, N. Ohsako, M. Iwamoto, Mechanical and shape memory behavior of composites with shape memory polymer, Compos. A: Appl. Sci. Manuf. 35 (9) (2004) 1065–1073.
[41] X. Lan, Y. Liu, H. Lv, X. Wang, J. Leng, S. Du, Fiber reinforced shape-memory polymer composite and its application in a deployable hinge, Smart Mater. Struct. 18 (2) (2009), 024002.
[42] K. Gall, M. Mikulas, N.A. Munshi, F. Beavers, M. Tupper, Carbon fiber reinforced shape memory polymer composites, J. Intell. Mater. Syst. Struct. 11 (11) (2000) 877–886.
[43] J.D. Ferry, Viscoelastic Properties of Polymers, John Wiley & Sons, 1980.
[44] V. Kaymenaki, Numerical & Experimental Investigation of the Behavior of SMP Structural Joints, (MSc Dissertation) Delft University of Technology, 2018.
[45] K.P. Menard, Dynamic Mechanical Analysis, a Practical Introduction, CRC press, 2008.
[46] N. Ni, Y. Wen, D. He, X. Yi, Z. Zhao, Y. Xu, Synchronous improvement of loss factors and storage modulus of structural damping composite with functionalized polyamide nonwoven fabrics, Mater. Des. 94 (2016) 377–383.
[47] D.J. Inman, Engineering Vibrations, Pearson Education, New Jersey, 2009.